Oxidation of a zirconium nitride multilayer-covered knee implant after two years in clinical use

Acta Biomaterialia 190 (2024) 593–604

Contents lists available at ScienceDirect

Acta Biomaterialia

journal homepage: www.elsevier.com/locate/actbio

Full length article

Oxidation of a zirconium nitride multilayer-covered knee implant after two years in clinical use

Julia S. Rau [a,*], Gustav Eriksson [b], Per Malmberg [b], Ana Laura Puente Reyna [c,d], Jens Schwiesau [c,d], Martin Andersson [b], Mattias Thuvander [a]

[a] Department of Physics, Chalmers University of Technology, Gothenburg SE-412 96, Sweden
[b] Department of Chemistry and Chemical Engineering, Chalmers University of Technology, Gothenburg SE-412 96, Sweden
[c] Aesculap AG, Research & Development, Tuttlingen DE-78532, Germany
[d] Departement of Orthopaedic Surgery, Physical Medicine & Rehabilitation, Ludwig Maximilians University Munich, Campus Grosshadern, Munich DE-81377, Germany

ARTICLE INFO

Keywords:
Tribologically-induced oxidation
ZrN
Knee implant
Transmission electron microscopy
Atom probe tomography

ABSTRACT

The surface composition and microstructure of an up to 5 μm thick multilayer on a knee implant were investigated. When the implant was explanted after approximately two years of clinical use due to failure from aseptic loosening, the topmost ZrN layer was found to be oxidized. Interestingly, only the non-articulating area was visibly oxidized (color change).

Up until then, the formation and characteristics of the oxide and its influence on the tribological performance remained uncertain. The oxide was thoroughly analyzed using transmission electron microscopy (TEM) and atom probe tomography (APT). The articulating and non-articulating areas were compared with an as-fabricated implant, which served as a reference. The results show that a thin oxide was also present on the articulating surface. All measured oxides were thicker than expected from native oxidation. The oxygen content of the majority of the oxide, measured with energy dispersive X-ray spectroscopy (EDS) and APT, was lower than required for the stable ZrO_2 form. Underneath the oxide, the ZrN layer remained unaffected, demonstrating the oxide's effective passivating behavior against further oxidation. No cobalt from the substrate was detected within the ZrN layer, proving the multilayer's excellent barrier function against ion release from the base metal.

Statement of significance: In our aging society, the use of artificial knee implants is widespread. Implant failure is not only costly, but often connected with pain for the patient and inevitably involves the implantation of a new joint. Hence, understanding the origin of joint failure is of high importance to extend the lifetime of the implant. In this research, we investigate the influence of a surface oxide, formed on an explant which failed after ~ 2 years, on the multilayer stability. As a novelty, we focus not on the wear of the polyethylene gliding surface but on the formed oxide. The use of high-resolution analysis techniques allowed us to get a glimpse on the ongoing mechanisms at the explants surface.

1. Introduction

In our aging society, total knee arthroplasty (TKA) is worldwide among the most common surgical procedures [1]. Over the last few decades, improvements in implant materials, such as surface modifications and coatings [2–4], have significantly contributed to their longevity and effectiveness. Coatings are applied to improve the tribological performance, biocompatibility and to reduce or prevent the release of metal ions from the implant into the surrounding tissue [2–5]. These ions are suspected to "[…] contribute to the pathophysiological mechanism of aseptic loosening by stimulating both the immune system and bone metabolism through a series of direct and indirect pathways" [6]. The release of very high ion concentrations can contribute to adverse neurological or cardiac effects [7]. According to a recent study, aseptic loosening is the most common cause of revision in total hip arthroplasty [8]. For TKA, it is either the most or second most common reason, depending on the region [9].

Among commonly used knee implant coatings, a seven-layer coating system featuring an outer ZrN layer has demonstrated reduced wear [5,10] and lower metal ion release [2,3,5] compared to conventional

* Corresponding author.
E-mail addresses: julia.rau@chalmers.se, rau.julia@aol.com (J.S. Rau).

https://doi.org/10.1016/j.actbio.2024.10.034
Received 7 June 2024; Received in revised form 17 October 2024; Accepted 22 October 2024
Available online 23 October 2024

monolayer coatings or uncoated implants [11]. Therefore, it is suitable for patients with metal allergies or hypersensitivity [2,5,12]. This coating has been observed to undergo a color change due to oxidation. For instance, an explant removed from a patient after approximately two years due to aseptic loosening exhibited this change [13]. Such oxidation, seen as a color shift (e.g. from golden to dark grey/blue), is often observed for ZrN coatings [14–16] and is linked to variations in the O and N composition [17]. Interestingly, the color change was only noted on the non-articulating area of the explant [13]. In this context, the distinction between articulating and non-articulating area was based on whether the area on the femoral component was in contact with the polyethylene gliding surface or not. Oxidation marks were also observed in the articulating area of femoral components after 5 million cycles in *in-vitro* testing, simulating highly demanding knee activities [5].

Puente Reyna et al. [13] conducted a thorough study of a ZrN-coated knee explant and found no impact of the oxide on the underlying layers, nor any other severe mechanism which could have led to the failure of this multilayer. To date, it remains unclear how this oxide forms, what its nature is (whether it is an oxide or an oxygen-rich solid solution), and why it is only observed in the non-articulating area of the explant [13].

Oxidation of metals under tribological loading is commonly observed under various conditions and across a wide range of contacts [18–24]. Under mild loading conditions, it was associated with diffusional processes along defects such as dislocations and grain boundaries [21,22]. Depending on their nature, the formed oxides may change the friction and wear behavior [23]. Higher friction and wear may result from stiff and hard layers [25], while mechanically softer layers tend to result in reduced wear [26,27]. Brittle or very thick oxide layers might also spall-off from the surface [22]. Although frequently observed, it is somewhat surprising that the underlying fundamental mechanisms of tribologically-induced oxidation are still not completely understood.

In this study, we systematically investigated the oxide formed on a ZrN-multilayer coated knee explant that was removed from a patient after approximately two years due to early aseptic loosening. Due to this relatively short usage time, this particular explant, studied by Puente Reyna et al. [13], is well-suited for investigating the mechanisms involved in the tribological contact. In fact, studies have shown that 90% or more of knee replacements last at least 10 – 15 years [1,28]. Puente Reyna et al. [13] already performed EDS, calo tests, and roughness measurements on this explant. Contrary to numerous previous studies, the present work specifically focuses on the femoral component and not on the wear at the polyethylene (PE) gliding surfaces [3,5]. This study aims to thoroughly investigate the oxide and its possible formation mechanisms using near-atomic high resolution analysis methods, including TEM and APT. Understanding the underlying mechanisms at the implants' surface within the human body is of high importance to extending the lifetime of TKA and preventing further revisions. These revisions are not only costly [29] but also result in physical and psychological impairment [30–32] and typically lead to worse outcomes than primary surgeries [1].

2. Experimental

2.1. Materials

Two AS VEGA System® femoral components were used: one as-fabricated implant and one explant (provided by Aesculap AG, Tuttlingen, Germany). Each consists of a CoCrMo base metal (material composition according to ISO 5832–4:2014) covered with a 3.5 – 5 µm thick multilayer (thin adhesive Cr layer, five alternating intermediate layers (CrN, CrCN) and a final topmost ZrN layer, Aesculap® AS Advanced Surface) [3,13]. The multilayer, fabricated by a physical vapor deposition (PVD) coating technology, has demonstrated increased longevity (reduced wear) [5,10] and reduced negative body responses and metal ion release [3,5,33] compared to conventional monolayer coatings and uncoated implants [11].

The explant, removed from a male patient (72 years, 1.8 m, 102 kg), was revised after two years of clinical use due to implant loosening. During the original surgery, the implant was affixed with bone cement (polymethyl metacrylate (PMMA) + ZrO_2, Palacos *R* + *G* bone cement, Heraeus Medical GmbH, Wehrheim, Germany) and combined with a ultra-high weight molecular polyethylene (UHMWPE) gliding surface [3,34]. After extraction, the UHMWPE gliding surface exhibited third body imprints, possibly from bone or bone cement particles [13]. The wear behavior of the UHWMPE gliding surface is not the focus of this study as it has already been examined by Puente Reyna et al. [5] and Grupp et al. [34].

The *in vivo* conditions, such as joint motion characteristics, starting conditions, and loading duration and sequences, remain unidentified or unknown. After explant removal in May 2020, the femoral component was rinsed with saline solution, gamma sterilized twice (total dose of ~ 60 kGy), cleaned for 30 min in an ultrasonic bath in ethanol, and eventually stored in air [13]. Puente Reyna et al. performed scanning electron microscopy (SEM), EDS, roughness analysis and applied two ball craters to visualize the multilayer structure on the explant [13]. The as-fabricated implant was stored in its original packaging, fixed in vacuum, and flushed with nitrogen until examination.

2.2. Microstructural and chemical characterization

Both the articulating and non-articulating surfaces were subjected to microstructural and chemical analysis. To fit the specimens into the SEM-chamber, the samples were cut using two types of low-speed diamond (wire) saws (Buehler IsoMet, Lake Bluff, USA and Well diamond wire saw SA, Switzerland) depending on the length of the cut. They were then cleaned for 15 min in ethanol and acetone. The TEM and APT specimen extraction was performed at a sufficient distance from the cutting surfaces (> 1 cm) to minimize possible influences such as deformation or heat evolution.

For the APT specimen preparation, a dual beam SEM/FIB (FEI Versa3D LoVac DualBeam) was used. Focused ion beam (FIB) milling techniques allowed for the preparation of specimens containing the region of interest, for example the oxide and the underlying ZrN. The sample's surface was protected by a 200 nm protective cap-layer, applied using a sputter coater (Leica EM ACE600, Leica Microsystems, Wetzlar, Germany). Three different coating materials were tested (Pt, Au, Cr).

APT specimens were characterized using the local electrode atom probe (LEAP) 6000 XR from Cameca (Madison, USA). By field evaporating ions from the very sharp, needle-like specimens, the local chemical composition of the samples was measured. The implementation of pulsed laser technology makes the investigation of poorly conducting materials, such as oxides, feasible [35]. The setpoint temperature was 50 K. Laser pulsing APT was conducted for all samples with a laser pulse frequency of up to 200 kHz, a laser pulse energy of 100 pJ and a detection rate of 0.5 - 1%.

Each data set or sub-volume (e.g. to specifically examine the oxidized region) was individually ranged using the commercially available AP Suite 6.3 software (Cameca). An evaporation field of 28 V/nm (representing Zr), an image compression factor of 1.65 and a field factor of 3.3 were used for all reconstructions. No information about the crystallographic planes was available from the datasets; therefore, default values were used. For bulk composition measurements, the built-in peak decomposition tool was employed to solve the overlaps between e.g. ZrN^{+}/ZrO^{+}, ZrN^{2+}/ ZrO^{2+} as well as Cr^{+}/ZrN^{2+} (see Fig. A11, supplementary information (SI)). For all shown datasets, the peaks were ranged with the dominating species (i.e. ZrN in the nitride and ZrO in the oxide). If these overlaps are not properly considered, the composition may not be accurate [36]. The 1D-composition profiles are presented decomposed and background corrected. Hydrogen was not ranged, as it originates from the sample preparation procedure and is present within the atom probe instrument vacuum chamber [37].

TEM specimens were prepared by FIB milling and analyzed using STEM with a FEI Titan 80–300 operated at 300 kV. EDS measurements (Oxford X-sight detector, Oxford Instruments) were conducted to cover a larger area than possible with APT (tilt angle of 15°, spot size 1). Quantification was performed with the TEM Imaging & Analysis (TIA) software, using a foil thickness of 100 nm and an averaged density of 6 g/cm^3. A map of the oxide on the explant's non-articulating area was created using an image size of 25 × 10 voxels and a dwell time of 2.5 s.

A time-of-flight secondary ion mass spectrometry (ToF-SIMS) instrument (ToF-SIMS 5, IONTOF GmbH, Germany), equipped with a Cs^+ beam as sputter gun and a 30 keV bismuth liquid metal ion gun (LMIG) as a primary source, was used to study the surfaces of the as-fabricated implant and non-articulating area of the explant more thoroughly. In addition to the surface spectra of both samples, a depth profile in negative ion mode on the explant's non-articulating area was measured using 1 keV Cs^+ ions for sputtering. The analysis current was 0.38 pA and the sputter current 79.48 nA. More details can be found in the SI.

2.3. Statistical analysis

One as-fabricated implant and one explant were investigated. SEM, TEM, APT and ToF-SIMS analyses were performed at the same locations (black boxes in Fig. 1). Two TEM-foils were cut and 2 - 4 APT specimens were prepared and analyzed at each location. The error stripes for the APT results originate from the commercial AP Suite 6.3 software (Cameca). Top-down EDS results of the explant's surfaces were averaged from four measurements.

3. Results and discussion

The focus of this study was on the outer ZrN layer and topmost oxide of a multilayer coating used in TKA. A thorough analysis of the whole multilayer will be performed in a future study. As previously stated by Puente Reyna et al. [13], at no time, "[…] delamination, flaking, roughening, deep scratches nor complete worn out of coating were seen, as no significant signal of all the base materials (Co, Cr, Mo) together with a complete disappearance of zirconium was detected". This demonstrates the previously reported wear behavior [3,5] and stability of the multilayer [11]. In this study, no Co or Mo were detected within the ZrN, supporting the previously observed excellent barrier function of the multilayer coating. Hence, this study aims to understand the nature of the oxide, its possible formation mechanisms, and its influence on tribological performance.

3.1. Optical impression

Photographs of the as-fabricated implant and explant investigated in this study are shown in Fig. 1. A homogenous, golden ZrN coating is present on the as-fabricated implant, which served as a reference. The explant shows a difference in color between the articulating (golden) and the non-articulating (greyish/purplish) area, as well as scratches at the articulating area (red arrows) and the transition between both areas. Due to the high reflectivity of the femoral components' surface, reflections of the surroundings (e.g. the imaging light, black arrows) are visible on both the as-fabricated implant and the explant. Puente Reyna et al. observed that for the lower red arrow in Fig. 1c, the CrN layer came through [13]. As this work focuses on the oxide formation on the ZrN, the locations highlighted with the red arrows were not investigated further. In the following, the areas on the explant will be abbreviated with art. and non-art. area.

3.2. Overview multilayers and oxides

In Fig. 2, TEM micrographs provide an overview of the multilayers for the three locations marked in Fig. 1a+b. The protective Pt-cap layer applied during sample preparation in the FIB was partially disconnected or spalled off from the surface during the final milling steps (Fig. 2a). To avoid this detachment, a circle was milled around the region of interest before Pt deposition to release surface tension during sample preparation (see SI1).

Fig. 2a, d, h show the entire multilayer, while Fig. 2b,c,e–g,i–k depict close-ups of the surface and the oxides. Multilayer thicknesses were measured in Fig. 2a,d,h. The total AS-layer thickness for the as-fabricated implant was 4.4 µm (2.3 µm for the ZrN-layer and 2.1 µm for the CrN—CrCN-layers). For the explant, the total layer thickness was 4.1 µm (art. area, 2.1 µm for the ZrN-layer; 2.0 µm for the CrN—CrCN-layers) and 4.2 µm (non-art. area, 2.1 µm for the ZrN-layer; 2.1 µm for the CrN—CrCN-layers). Fig. 2b,c,e–g,i–k will be discussed in more detail in the following chapters.

3.2.1. As-fabricated implant

Surface: A very thin oxide layer (1 - 3 nm) was formed on the surface (Fig. 2b,c). APT analysis of the as-fabricated implant suggests a similar observation: the surface and bulk regions are depicted in Fig. 3. The sample surface is marked by the sputtered Pt layer (black dots) (Fig. 3a). The implant's surface contains up to 5 atomic percent (at%) of oxygen, which could indicate a very thin (few nm) native oxide layer (Fig. 3d). As the oxygen-containing regions are very small for this sample, no separate ranging for the oxygen-rich area was performed. Due to the ZrN/ZrO overlaps in the mass spectrum (Fig. A11, SI), the absolute

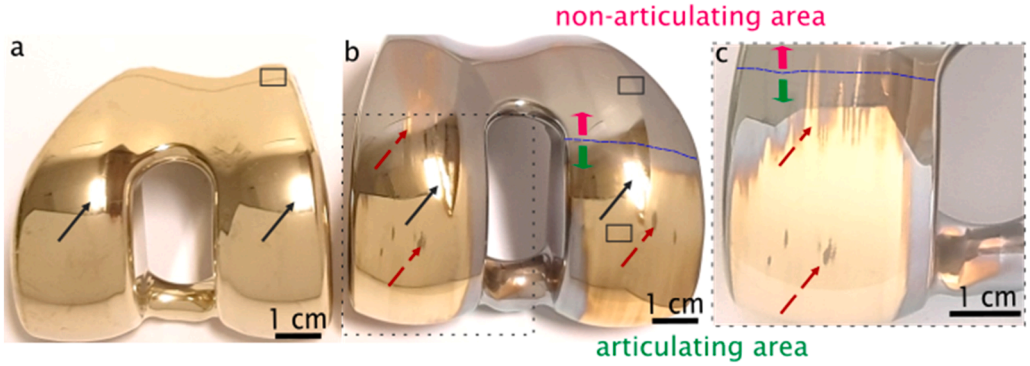

Fig. 1. Photographs of (a) as-fabricated implant, (b) explant and (c) different view angle and higher magnification image on the area marked in (b). The as-fabricated implant shows no scratches or inhomogeneities of the coating. Visible features are due to reflections during imaging, caused by the polished surface of the femoral components. For example, black arrows mark the reflection of the imaging light. Red arrows indicate actual features on the explant's surface. Solid black boxes represent the locations where the cross sections, TEM-foils and APT specimens were taken from. Areas in contact with the gliding surface are defined as articulating areas. The articulating and non-articulating areas are roughly separated by blue dashed lines.

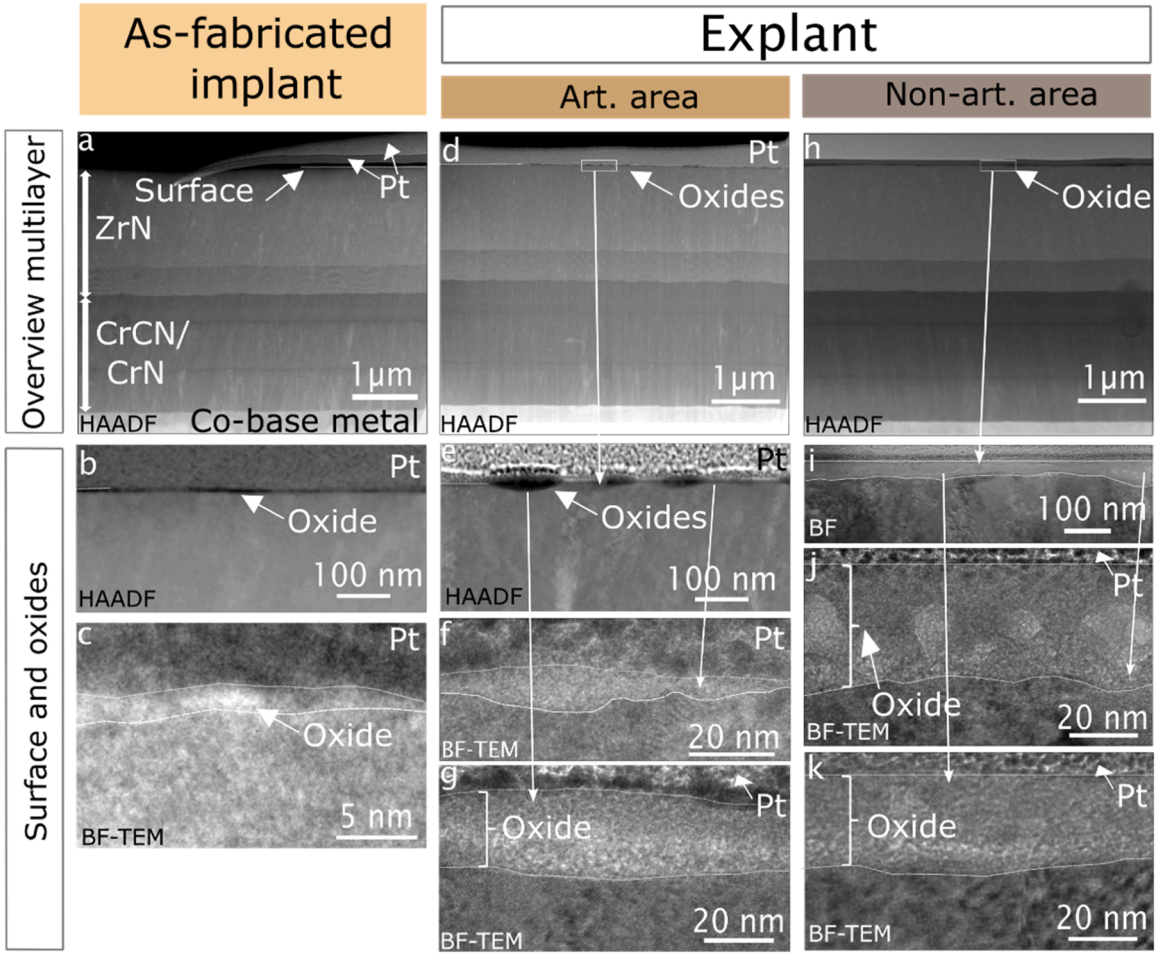

Fig. 2. (S)TEM-images of the multilayer on the femoral components show a ZrN layer on top of five alternating CrN and CrCN layers. (a–c) As-fabricated implant, (d–g) art. area and (h–k) non-art. area on the explant. (c,f,g,j,k) bright field (BF) images in transmission mode, (a,b,d,e,h) STEM images in high angle annular dark field (HAADF) mode and (i) in BF mode. The surface was covered by protective platinum applied during the SEM/FIB sample preparation. The Pt-layer partially spalled off from the sample surface during final thinning as seen in (a). The surface is marked with a dashed line. (a,d,h) Overview of the entire multilayer, (b,c,e-g,i-k) close-ups of the surfaces focusing on formed oxides. (a) and (b + c) are from two different TEM-foils.

oxygen composition in Fig. 3a–d might be underestimated. Measuring the oxide stoichiometry with APT is challenging [38] and depends, for some oxides (e.g. MgO), on the laser pulse energy and applied voltage [39]. Under high field conditions, neutrals (e.g. O_2-carrying molecular ions) can form, leading to discrepancies in the stoichiometry [38]. For MgO, the correct stoichiometry was measured at low laser energies and high electric fields [39]. Using higher laser pulse energies from 100 – 250 pJ, Yu et al. measured a ZrO_2 composition in neutron irradiated ZIRLO™ [40], demonstrating that the parameters we used were suitable for detecting a ZrO_2 composition. Bachhav et al. used 70 pJ for analyzing a Zr-oxide/Zr interface and observed the presence of both ZrO and ZrO_2 [41].

The observation of the thin native oxide layer on ZrN is consistent with literature, where studies have reported a native oxidation layer (under ambient conditions) with a thickness of just a few nm [42–46]. For example, Muneshwar et al. reported a self-limiting surface oxidation process with a final oxide thickness of approximately 3.7 nm [46]. This thin surface layer comprises a mixture of zirconium oxide and oxynitride (varying N content).

An O ICS of 2 at% highlights a finger-like structure extending from the surface into the bulk (Fig. 3a+b). Such features could indicate a grain boundary with dislocation pipes decorated with oxygen [22,47,48]. This will be discussed in more detail in chapter 3.5.

Bulk: The bulk ZrN (Fig. 3e) shows a homogenous distribution of ZrN and O, with a 51:47 Zr:N ratio. The O content was below 1 at%. He et al. characterized ZrN coatings with STEM-EDS, electron energy loss spectroscopy (EELS) and APT, concluding that EELS and APT exhibited a "[…] higher reliability in determining the N/Zr ratio in the coating" than EDS [49]. For steels, the nitrogen content was significantly underestimated in the past [50,51], thought to be caused by multiple hit events [51] and overlapping peaks of Fe and N [50]. Here, the detected ratio of approximately 1:1 Zr:N does not show this trend and seems to correctly represent the expected composition. Among the observed elements, around 0.3 – 0.5 at% Hf is found (see Figs. 3e and A3). This element is frequently present in ZrN magnetron-sputtered thin films, as it is an impurity in Zr targets [52]. For example, Fernandez et al. [52] reported ~ 1 at% of Hf in "pure" ZrN films.

3.2.2. *Explant*

The explant shows oxide patches on the surface within the art. area (Fig. 2e–g), connected by a very thin surface oxide in between and a continuous surface oxide layer on the non-art. area (Fig. 2i–k). Within this layer, some areas with different contrasts are visible (Fig. 2j). The HAADF contrast is sensitive to atomic number: darker areas represent lighter elements, while brighter areas indicate heavier ones. From the BF-images, the thickness of the oxide on the non-art. area can be estimated as between 30 - 50 nm (Figs. 2i–k, A12g+h). The oxide thickness in the art. area varies between a few nms (~ 2 - 5) up to 25 nm in the patchy regions (Fig. 2f,g).

A reconstruction of the explant's art. area is depicted in Fig. 4. In

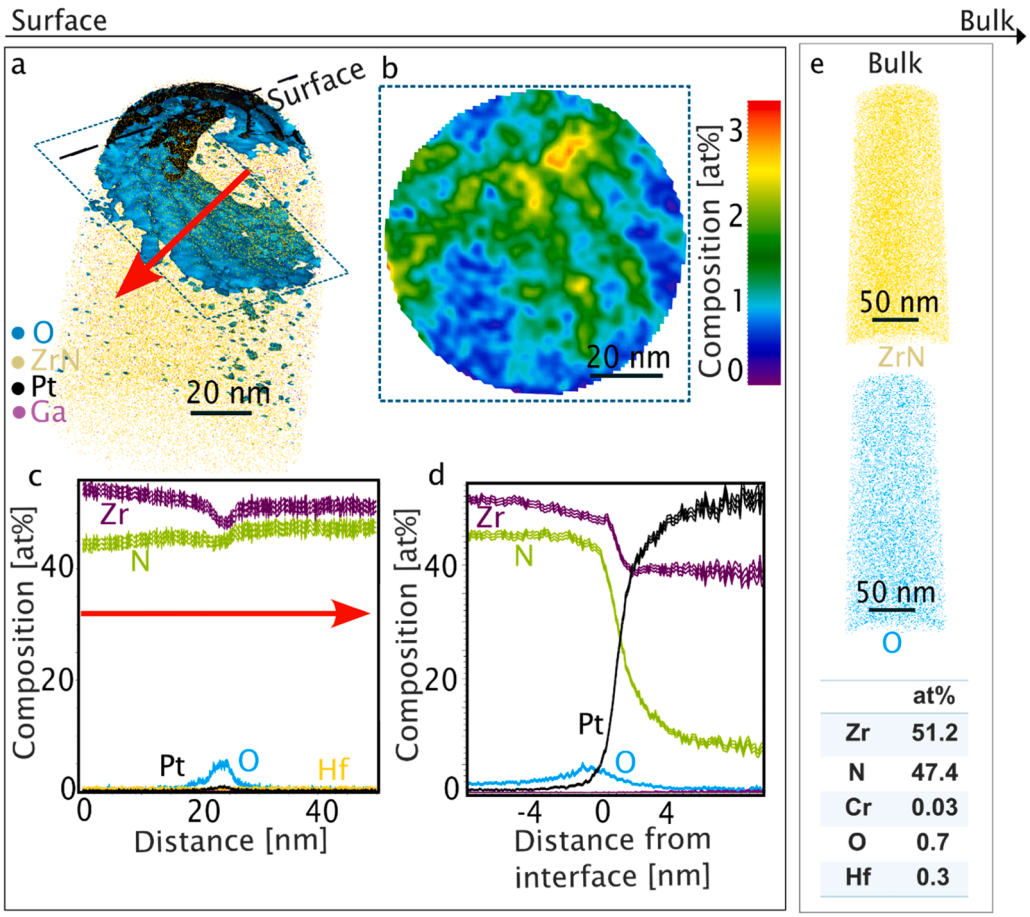

Fig. 3. APT analysis of the as-fabricated implant. (a-d) Surface and (e) bulk. (a) A three-dimensional reconstruction of the surface, where O atoms are represented as blue dots, Ga as purple dots, Pt as black dots and ZrN ions as yellow dots. Ga and Pt originate from the sample preparation (i.e. FIB and Pt capping layer) and are not part of the as-fabricated implant. The surface is marked by a dashed line. An oxygen iso concentration surface (ICS) with 2 at% is highlighted, revealing finger-like features extending from the surface into the bulk. These features are more visible in the 2D composition plot through the dashed area marked with the rectangle in (a) for the oxygen composition (b). (c) A 1-D composition profile across the finger-like features (indicated by the red arrow in (a), cylinder $d = 30$ nm) shows an enrichment of up to 6 at% of oxygen at the finger-like features. (d) A proxigram for a 10 at% Pt ICS (representing the protective Pt-capping layer on the surface) shows an enriched oxygen composition at the surface of up to 5 at%. (e) A section from the ZrN-bulk with 10 nm thin slices for the distribution of ZrN and O. The table depicts the decomposed bulk composition for this region with approximately 50:50 at% Zr:N.

Fig. 4a, a 5 nm thin slice through the whole measurement is shown. No Pt-cap layer could be detected, but a ~ 20 nm thick oxygen-containing surface layer is present. All oxygen-containing species are depicted as blue dots. With increasing depth, a Pt and Ga containing interface appears, followed by an area with elevated Cr concentration. Fig. 4b–d provide a more detailed look on the oxygen-containing surface layer. Fig. 4b depicts a 5 nm thin slice of the first 2 million ions with an O ICS of 2 at% representing the oxide/ZrN interface, allowing for comparison with the as-fabricated implant (Fig. 3). The O content within the oxide (Fig. 4c) reaches up to 50 at%, which will be discussed in the next chapter. The interface exhibits a sharp transition between the oxide and ZrN.

Fig. 4d represents a 1-D composition profile along the blue arrow in Fig. 4b. This was verified with two individually ranged regions above and below the interface to account for the ZrN/ZrO overlaps. The top of the specimen contains up to 20 at% of Ga and around 35 at% of O. Due to Ga contamination from the sample preparation, only the parts of the oxide with low Ga values are considered. This approach helps to avoid artifacts that could result from gallium damage [53]. As a result, the APT datasets from Figs. 4 and A3 are mostly used to investigate the ZrN bulk composition and to gain insights into the oxide/nitride interface. From the APT datasets, it is not possible to determine the oxide thickness, as the exact position of the surface remains unclear. In addition, information about the individual crystallographic planes could not be assessed so the absolute thickness cannot be extracted. Since the same reconstruction parameters were used for all datasets, only a relative comparison for the explant's oxide thicknesses can be made. This comparison shows maximum thicknesses of 30 nm (non-art. area) and 40 nm (art. area). These values are within a comparable range to the thicknesses measured in the TEM micrographs. Compared to a native oxide (a few nms), the explants' oxides are thicker (10 - 50 times).

The table in Fig. 4 depicts the ZrN-bulk with the decomposed bulk composition for two individually ranged data sets within the ZrN- and Cr-rich area. The ZrN shows a 51:48 at% ratio between Zr:N whereas the Cr-rich area shows a 25:23:46 at% Zr:N:Cr ratio. The O content is slightly increased in the Cr-rich area (1.4 at%). Furthermore, some Co (1.5 at%) and C (1.9 at%) were found. The appearance of the Pt-enriched interface is discussed in the SI, chapter 3.

3.3. *Chemical composition and microstructure of the explant's oxides*

From the TEM-images in Fig. 2a, it is apparent that the native oxide is approximately 1 - 3 nm thick. Therefore, the focus is on the oxides on the explant, as the oxide on the implant was too thin to analyze in the same depth.

3.3.1. *Oxide composition*

To assess the chemical composition of the oxides, different

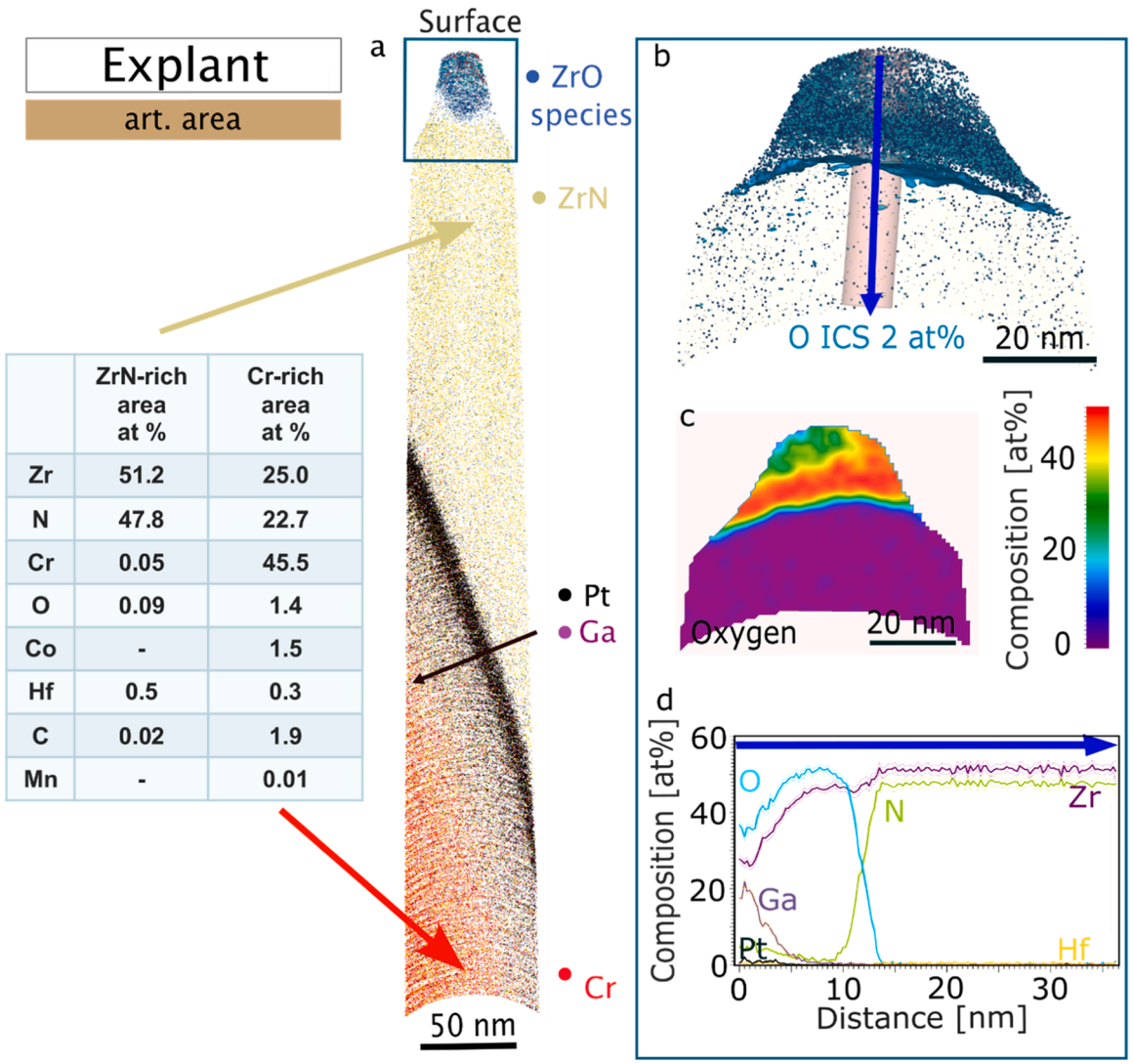

	ZrN-rich area at %	Cr-rich area at %
Zr	51.2	25.0
N	47.8	22.7
Cr	0.05	45.5
O	0.09	1.4
Co	-	1.5
Hf	0.5	0.3
C	0.02	1.9
Mn	-	0.01

Fig. 4. APT analysis of the explant's art. area. (b-d) Surface and (table) bulk composition. (a) A 5 nm thin slice of a three-dimensional reconstruction of the entire sample. Oxygen-containing species are depicted as blue dots, Pt atoms as black dots, Ga as purple dots, Cr as red dots and ZrN ions as yellow dots. Ga and Pt originate from the sample preparation and are not present in the explant itself. (b) 5 nm thin slice of the first 2 million ions, separately ranged (marked in (a)), representing the surface. The oxide-ZrN interface is marked by an O ICS of 2 at%, enabling comparison between the as-fabricated implant and explant. (c) A 2D composition plot of the oxygen composition from (b), indicating a ZrO composition in the red regions. (d) A 1-D composition profile across the boundary between oxide and ZrN from (b, blue arrow). The table represents the bulk composition of two separately ranged data sets, only within the ZrN- and Cr-rich areas, with decomposed peaks.

techniques were applied: APT, TEM EDS and ToF-SIMS. The APT results are shown in Figs. 3 and 4. TEM EDS and ToF-SIMS will be discussed in this chapter.

TEM EDS elemental mapping and point analyses were conducted on the surface layer of the explant's non-art. area (Fig. 5). The results of the point analyses are given in Fig. 5b. Two points with different gray values were chosen (see for example Fig. 2j). The measured O composition was ~ 38 - 39 at%. The maps in Fig. 5c, obtained from the marked region in Fig. 5a, show that the surface layer contains O. Quantification of light elements (e.g. C, N and O) with EDS is challenging and the elements' concentrations are often underestimated [54]. Moreover, overlaps of the peaks (such as between Cr and O) may influence the quantification. Therefore, the quantification of O and N should be taken with a grain of salt. The element-concentration profile shown in Fig. 5d indicates that the oxygen concentration within the oxide (first ~ 40 nm) varies between 40 and 50 at%.

ToF-SIMS was performed to study the as-fabricated implant and explant's surfaces with respect to the formed oxides (Fig. 6). The explant exhibited higher peaks for the oxygen-containing species than the as-fabricated implant (Fig. 6a). For these two spectra, the relative ion intensity normalized by ion dose for ZrO_2^- and ZrN^- is shown in Fig. 6b. For ZrO_2^-, the explant had a 2.7 times higher relative ion intensity than the as-fabricated implant. Additionally, the explant had a 10 times higher relative ion intensity for the ZrO_3^- compared to the as-fabricated implant. Conversely, the ZrN^- relative ion intensity was 54 times larger for the as-fabricated implant than for the explant.

In Fig. 6c, the sputtered depth was 15 μm (calculated from a SEM image). Assuming a linear sputter rate, the oxide would be approximately 800 nm – 1.6 μm thick (250 – 500 s), which does not align with the measured thicknesses from the TEM images. It is likely that the sputter rate through the oxide was slower than through the nitride. Thicknesses measured with APT and TEM are in a similar range and Puente Reyna et al. speculated that the oxide layer is only "some nanometer" thick, as determined using a ball crater technique [13]. Combining these three techniques underlies that the sputter rate during ToF-SIMS was probably different in the oxide.

Interestingly, the Zr^- curve remained almost constant, while the oxide and nitride-containing peaks showed a steeper decrease/increase.

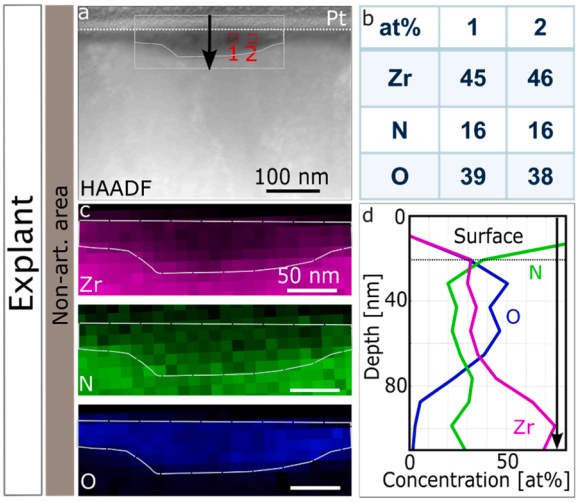

Fig. 5. STEM-EDS measurement of the surface layer on the explant's non-art. area. (a) HAADF-STEM overview of the surface layer. Point measurements were conducted at locations 1 and 2, as depicted in (b). (c) EDS maps of the area marked in (a) for Zr, N and O. (d) Element-concentration profile along the black arrow in (a) for Zr, N and O.

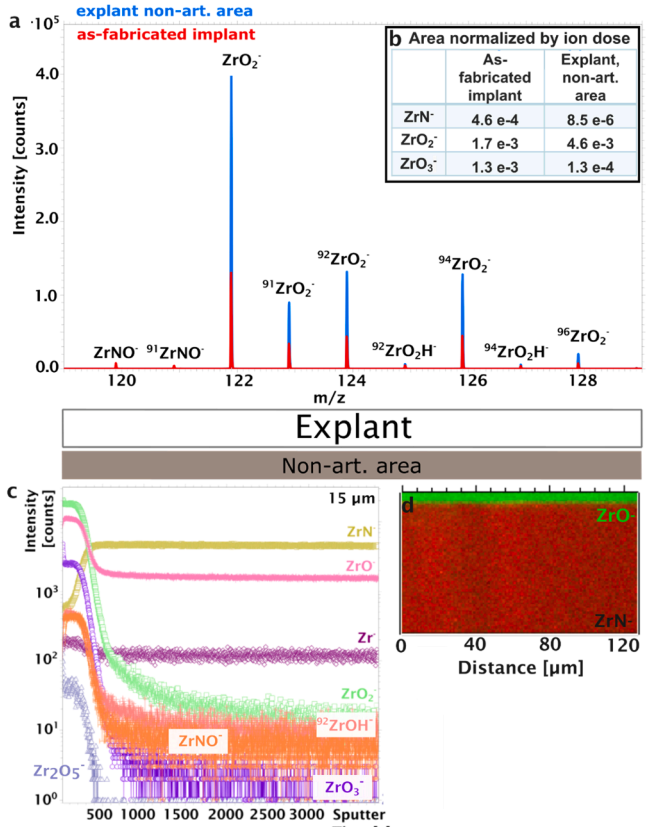

Fig. 6. ToF-SIMS analysis. (a) Comparison of the as-fabricated implant (red) and the explant's non-art. area (blue). The spectrum was obtained after a few seconds of sputter cleaning with Cs^+; negative ion mode using a Cs^+ source, focusing on the 119 – 129 *m/z* part of the spectrum. (b) Area normalized by ion dose for the as-fabricated implant and explant on the non-art. area for ZrN^-, ZrO_2^- and ZrO_3^-, calculated from the spectra in (a). (c) Depth profile for the explant (non-art. area), sputtered for 4700 s, showing only selected oxide species. (d) Overlay of the X-Z slice of ZrN^- and ZrO^- from the depth profiling.

Overall, the ToF-SIMS measurements reveal a variety of zirconium oxide species present within the spectra, as it was conducted over a relatively large area (127 × 127 µm^2). This reflects all ion species within these regions, covering multiple oxide phases at the very top monolayers of the material. ToF-SIMS is not a quantitative method for determining oxide composition, but it can provide important qualitative insights. The oxide layer is dominated by ZrO, with signals also indicating the presence of ZrO_2 and ZrO_3 (Fig. 6b). The bulk is dominated by ZrN (Fig. 6c+d). The sum of these zirconium oxide species indicates the complex nature of the oxide on the explant [55].

Table 1 summarizes the results for the oxide composition obtained from different techniques, excluding ToF-SIMS for the reasons discussed above.

STEM-EDS showed an oxygen concentration of up to 50 at%. In comparison, Puente Reyna et al. [13] found ~ 1 – 2 at% of O in the art. area and ~ 22 at% in the non-art. area. However, the detection of Cr indicates that the acceleration voltage was high enough to measure the underlying Cr layer, suggesting that the composition is not representative of the top oxide layer. Additionally, there was a significant C contamination on the surface. Up to ~ 1 at% of Cr was also detected in the SEM-EDS measurements in this work (Table B1) with a Zr:N:O ratio of 44:45:10 at% in the art. area and 46:10:44 at% in the non-art. area.

Formed oxides on Zr or ZrN are studied in a variety of conditions and applications. The most stable oxide is ZrO_2 (lowest formation enthalpy) [56,57], which has different structures depending on the temperature. Other groups report the formation of Zr_3O or ZrO but they require higher temperatures to form [57–59]. Until a few years ago, no stable structure of ZrO was known. Through a combination of experimental techniques and theoretical structure predication, Nicholls et al. suggested a hexagonal ZrO structure present at the Zr-ZrO_2 interface in nuclear fuel claddings (at 360 °C with simulated primary water) [57]. This structure provided the smallest mismatch of 2 % at the boundary. Ni et al. observed the presence of ZrO as well, using EELS (360 °C) [59]. To the best of the authors' knowledge, ZrO has not been found at room temperature so far. In addition, the presence of gradients within the oxides is often reported (e.g. a sub-oxide formed at the metal-oxide interface) [57, 59]. When staying below 450 °C, Milošev et al. reported that an oxynitride film is formed where some N remains trapped [43]. It is only when temperatures exceed 450 °C, that N is fully released forming a pure oxide layer on ZrN.

The composition of ~ 50 at% O within the oxide on the explant, measured with APT and EDS (Figs. 4c+d and 5d), suggests the formation of ZrO. One explanation for observing ZrO in the APT data could be the setup of the analysis. When measuring the oxygen composition in an oxide using APT, it is important to consider the influence of the field on the specimen. When the oxide sits on top of the metal or nitride, a thin ZrO layer (~ 10 nm) has been found at the interface due to a migration of oxygen towards the interface [60]. It could be possible that the same phenomenon occurred in this case as well. Furthermore, it might be the case that the topmost ZrO_2 and ZrO_3 layers (observed with ToF-SIMS) have spalled off from the surface before it could be detected (Fig. A4). In the present study, it seems that the majority of the oxides had lower oxygen content than ZrO_2 (67 at% O) and some remaining N. One possible explanation could be, that the temperatures reached in the tribological contact were not high enough to form ZrO_2.

Table 1
Overview of the chemical composition of the oxides on the explant. The SEM-EDS results are taken from [13] and Table B1.

Method	Unit	Area	Zr	N	O	C	Cr
STEM-EDS	at%	non-art.	30 - 46	16 - 26	38 - 50	–	–
SEM-EDS [13]		non-art.	28	13	22	36	0.4
		art.	30	20	2	39	3
SEM-EDS		non-art.	46	10	44	–	0.4
(Table B1)		art.	44	45	10	–	1
APT		art.	45	2	52	–	–

3.3.2. Oxide microstructure

High resolution BF TEM images allow for the identification of differences within the oxides on the explant, as shown in Fig. 7. Here, ring-like patterns and diffraction spots appear when plotting the fast Fourier transforms (FFTs) from the marked areas. The red squares represent the ZrN and show diffraction patterns. Green and blue squares are taken from inside the oxide. Ring-like patterns without any diffraction spots indicate amorphous regions within the oxides whereas the presence of some diffraction spots (in the blue square) indicates some (nano-) crystalline regions. For all investigated surfaces, the nano-crystalline areas seem to be present closer to the nitride/oxide interface than the surface. The thin oxide layer in between the patches (art. area) was found to be amorphous (Fig. 7e+f). These observations indicate, as discussed above, that the oxygen composition (< ZrO_2 composition) is insufficient to form a stable oxide, resulting in this meta-state.

3.4. Art. area vs. non-art. area

From the previous chapters, the following differences between the art. and non-art. area can be observed. The different colors in Fig. 1b+c indicate different surface compositions for the art. and non-art. areas [14–16]. The art. area seems to be polished (golden color) and exhibits scratches. Puente Reyna et al. found Cr within the scratches, indicating the complete removal of the top ZrN layer [13]. They speculated that the "[…] articulating areas were polished by bone cement particles embedded in the polyethylene gliding surface" [13].

The multilayer appearance of the art. and non-art. areas is the same (Fig. 2d+h), except for the oxide layer at the surface. When analyzing all atom probe datasets within the ZrN bulk region, a ratio of ~ 51:47 at% Zr:N was found (Figs. A3 and 4), which is comparable to the as-fabricated implant. A slight difference in the O composition between the art. and non-art. area is observed (0.4 – 0.9 at% vs. 0.4 – 0.5 at%), see Fig. A3. In total, the subsurface ZrN composition was not noticeably influenced by the tribological loading or exposure to body fluids. The most significant difference between the art. and non-art. area is the near-surface part with an oxide formed on both locations (Figs. 2d–k, 4, 7 and A3). The oxides in the art. area are smaller and patchy, whereas the oxide in the non-art. area is continuous and thicker. The APT data from Fig. 4 reveals that the patches in the art. area are oxides with an oxygen composition of up to ~ 50 at%. The observation of this oxide layer is somewhat surprising, given that the color of this area does not indicate an oxide (Fig. 1b). The patchy nature seems not to be sufficient to change the color. The following chapter discusses the possible origins of these oxides.

3.5. Origin of the oxides

The oxides on the explant were thicker than expected from native oxidation [42,43,45]. Such thicker oxides can result from increased temperature, exposure to a corrosive medium, tribological loading or combinations of these factors.

3.5.1. Temperature

Increased temperatures significantly influence oxide formation, for example, annealing ZrN films for 4 h at 450 °C resulted in a 22 nm thick oxynitride layer [43]. Harrison et al. found ~ 25 µm thick oxide layers when heating ZrN to 900 °C for 5 h [61]. To the best of the authors' knowledge, no experiments have been conducted at body temperature without any other influencing factors to measure the resulting oxide thickness. It is expected that the thickness would lie within the range of native oxidation, as surfaces under ambient conditions may experience some temperature variations that could lead to temperatures equivalent to body temperature.

3.5.2. Corrosive medium

Almost every material in contact with a biological system will exhibit some degree of bio-corrosion [6]. For example, Brown et al. observed oxide formation when exposing a ZrN layer to 0.5 N NaCl in distilled and deionized water for in total 90 days [15]. Associated with the oxide formation, the color in some cases changed to a slightly bluer tinge [15]. They concluded that this oxide layer, formed by the replacement of N at the surface with O, possesses good corrosion resistance and is protective. Using X-ray photoelectron spectroscopy (XPS), the "[…] unexposed layer containing oxygen above the background level was 392 Å thick", whereas after 50 days of exposure, the oxygen-containing layer had a thickness of 1635 Å [15]. Formed oxides on ZrN (i.e. ZrO_2 and zirconium

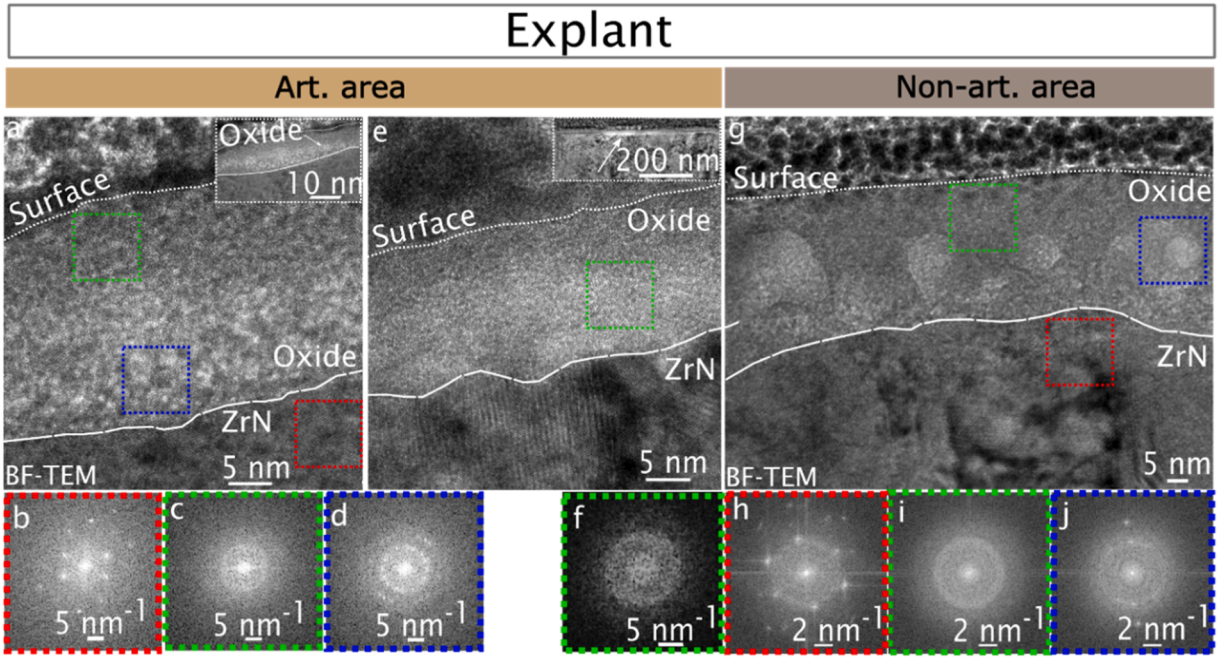

Fig. 7. BF-TEM images of the explant (a,e,g). (a–f) art. area and (g–j) non-art. area. The surface and oxide/nitride interface are marked by dashed lines. (b–d, f, h–j) FFTs from the regions marked in (a,e,g). Inserts in (a) and (e) show the locations where the FFTs are taken from.

oxynitrides) are usually protective or more resistant to further corrosion [15,44,62,63]. It is reasonable to expect that the oxide layer on the non-art. area results from oxidation occurring within the corrosive environment of the human body.

3.5.3. Tribological loading

In metallic contacts, tribological loading is known to generate oxides thicker than those expected from native oxidation [21,22,64]. For example, a factor of 470 thicker oxide under tribological loading has been observed for copper [22], compared to 10 – 50 times thicker oxides that were observed on the explant. Shear stresses may influence the reaction enthalpy and enhance tribochemical reactions for various reasons, including localized heating, mechanical activation and surface renewal [65–67]. Tribo-oxidation of nitride films has been observed in a variety of different contacts [68–70]. For instance, Luo et al. found "[…] the formation of a nanocrystalline/amorphous multicomponent oxide tribofilm strongly attached to the worn surface" on a TiAlN/VN layer [68]. Oxide formation on ZrN is in general beneficial for the tribological properties, as it increases wear resistance and decreases the coefficient of friction [66–68,71].

For the explant, a clear difference between the art. and non-art. area is observed, as wear was not only limited to the softer UHMWPE gliding surface but also clearly appeared on the art. area. Wear of the non-PE component of a knee implant setup has previously been observed: approximately 12 wt% of the wear products were metallic, likely stemming from the femoral component [72]. For the explant, the Cr-containing layer broke through in the art. area (Fig. 1b+c (lower red arrow)) [13]. This indicates the presence of abrasive particles in the contact zone. Indeed, Puente Reyna et al. observed Zr and O-containing particles imprinted in the UHMWPE gliding surfaces [5]. They speculated that these particles stem from the contrast medium of the bone cement (ZrO_2) and constantly polished the art. area. The size of this embedded particles was on average 2.65 ± 2.49 μm (half of all particles had a size between 1 – 2 μm, Fig. A9) which is larger than what would result from oxides removed from the explant's surface. So even if the formed oxide on the explant's art. surface would be removed, its size would be smaller than the already present bone cement particles. Another possible source of the abrasive particles could be abraded growth defects from the multilayer (Figs. A5–8). These growth defects are discussed in more detail in the SI in chapter 3.

3.5.4. Combinations of temperature, corrosive medium and tribological loading

When combining two or more of the above-mentioned influencing factors, their synergistic effects become apparent. For example, Pejakovic et al. studied the tribological performance of zirconium-based nitride coatings exposed to a Na_2SO_4 aqueous solution and found enhanced wear resistance based on the "[…] ability to form a stable oxide layer with a thickness of a few hundred nanometers" [73]. Exposing a TiZrN coating to Hank's solution with and without calf serum at 37 °C under tribological loading resulted in the formation of a stable Ti, Zr oxide or oxynitride layer, which improved friction and wear behavior [74]. Oxidation of ZrN-coated knee implants has been reported in both *in-vitro* and *in-vivo* studies [5,13].

Overall, there are two main possible mechanisms for the oxidation of the explant's surface: (1) Oxidation due to the corrosive environment of the entire surface (referred to as static oxidation, as no mechanical influence is expected), and (2) static oxidation on the non-art. area and tribologically-induced oxidation on the art. area. At this point, it is not possible to exclude either mechanism with certainty. In both cases, continuous removal of the formed oxide and topmost ZrN layer on the art. area occurs, as the CrN layer has already broken through in some locations. A possible mechanism could be abrasion via embedded particles within the PE matrix [13]. These particles could originate from bone cement (ZrO_2) or abraded growth defects from the surface. A detailed analysis of these particles would be required to clarify their origin.

Based on the nature of the formed oxides, mechanism (2) seems more likely. Firstly, to the best of the authors' knowledge, an oxygen containing layer always forms on ZrN under tribological loading due to its oxygen affinity. Secondly, it is unclear if the art. area has sufficient accessibility to the corrosive media at the surface. Thirdly, if the oxide on the art. area were purely of static origin, it would not be present with this thickness within the art. area, as it would have been removed under sliding. Since tribologically-induced oxides grow much faster than under static conditions [22], an oxide can reform under loading conditions after being worn off. Lastly, with mechanism (1) the interface between nitride and oxide would be expected to look the same as the oxide on ZrN grown on this interface (a continuous layer with relatively straight interface). From the TEM-images shown in Figs. 2d–g and A12c–e, the oxides on the art. area form individual patches connected by a very thin oxide layer. This thin layer could have formed due to native oxidation after removing the explant from the human body. This difference in the oxide's appearance indicates two different formation mechanisms for the art. and non-art. area.

Patchy or cluster-like oxide formation under tribological loading within the subsurface area was previously reported in high-purity copper in dry contact with sapphire [21,22,24,64]. Here, the accelerated oxide formation was associated with dislocation pipe diffusion (oxygen entering the material and copper diffusing to the surface). Dislocation pipes decorated with oxygen were found within the pure metal as well as the formed oxide [22]. The relatively sharp interface between oxide/-nitride shows no evidence of pipes reaching into the ZrN. However, the finger-like features on the as-fabricated implants' surface (Fig. 3b) indicate oxygen enrichment at dislocations. Stiller et al. also reported the presence of oxygen-enriched finger-like structures within zirconium oxide formed in a nuclear reactor [35]. The tribologically-induced oxidation in copper was mainly associated with dislocations and their movement [22]. Nitrides exhibit significantly reduced plasticity compared to copper. Nevertheless, recent studies have shown appreciable dislocation mobility at room temperature for various ceramics, as summarized by Fang et al. [75]. For example, Wu and coworkers studied the nanoindentation-induced plastic deformation in a nanocrystalline ZrN thin film (2.2 μm) [76]. The dislocation density within the deformed zone was $\sim 3 \cdot 10^{12}$ cm^{-2}. For metals, Greiner et al. detected geometrically necessary dislocation densities in the order of $4 \cdot 10^{10}$ to 10^{12} cm^{-2} in copper after one pass of a sapphire sphere which is comparable [77]. Oxygen transport is not only faster along dislocations but also occurs orders of magnitude faster via grain boundaries than through the bulk [78]. As PVD layers exhibit columnar growth structures, these columnar boundaries may serve as additional diffusion pathways for oxygen. The microstructure of the oxides (Fig. 7) shows nano-crystalline areas closer to the oxide/nitride interface and amorphous regions closer to the surface. This could indicate more oxygen closer to the oxide/nitride interface which starts to form these nanocrystals. For the oxidation of Zr, the diffusion/transport of oxygen through the oxide occurs faster than the movement of Zr towards the surface, supporting this finding.

Other fast transport pathways involve phase boundaries, free surfaces and/ or cracks. As the multilayer contains some growth defects, with some protruding from the surface, these less densely packed or empty interfaces might serve as transport pathways. The enrichment of Pt, Ga, C and O, as observed in the APT dataset in Figs. 4 and A8 indicates such an interface allowing for material transport (discussed in more detail in chapter 3, SI).

Overall, an equilibrium might be evolving at the art. surface following three steps: (I) an oxide forms through a combination of corrosion and tribological loading. Defects may serve as faster pathways for oxygen and corrosive media to enter the surface. Such defects could be the interface between growth defects and coating (see chapter 3, SI), dislocations, and columnar grain boundaries. (II) Meanwhile, bone cement particles embedded into the gliding surface lead to abrasion of the formed oxide/ZrN layer. Growth defects, now exposed to the

surface, might be pulled out and embedded into the UHMWPE. (III) Embedded particles within the UHMWPE remove the formed oxide and introduce new defects, allowing for continuous oxidation. Meanwhile, the oxide on the non-art. area will grow without the influence of tribological loading, which will occur rather slowly due to the protective nature of the oxide.

5. Conclusions

The surface properties of a zirconium nitride multilayer-covered knee implant after two years in clinical use were studied, focusing on the formation of oxides, their nature and possible influences on tribological performance. Based on SEM, (S)TEM, EDS, ToF-SIMS and APT analysis, the following conclusions can be drawn:

- The as-fabricated implant has a very thin native oxygen-rich layer on top of the ZrN layer.
- On the explants surface, an oxide was formed on the art. and non-art. area; both were thicker than expected from native oxidation. On the art. area, the oxides were patchy and thinner ($\leq$ 25 nm), while on the non-art. area, a continuous layer developed with a thickness of up to 50 nm. No Co was measured within the ZrN layer, indicating effective protection by the multilayer against ion diffusion from the substrate. The majority of the oxide had a concentration closer to ZrO (O $\lesssim$ 50 at%) than the more stable ZrO_2, indicating the complex processes occurring at the explant's surface.
- Cr-rich particles, likely growth defects from the PVD process, were present on all surfaces. The interface between the growth defects and the coating was discontinuous or less densely packed, allowing for faster material transport from the surface into the ZrN layer.
- Wear of the art. area seems to be caused by either ZrO_2 from bone cement or abraded growth defects, which become embedded into the UHMWPE gliding surface and cause abrasion of the oxide and multilayer within the contact.
- The most likely explanation for the differences in the oxide formation and appearance between the art. and non-art. area is static oxidation on the non-art. area and tribologically-induced oxidation on the art. area. The faster- growing oxide in the art. area is successively removed by the embedded particles within the gliding surfaces. As the oxide thickness was $\leq$ 50 nm, the influence of the removed oxide on the wear process is expected to be negligible compared with the bone cement particles and growth defects.
- Oxidation of the ZrN appears inevitable, yet the underlying ZrN layer remained unaffected, indicating that the formed oxides protect against further oxidation.

This study generates a deeper scientific knowledge about the surface structure and wear behavior of the implant coating and is not related to a failure mechanism of the coating. In the future, the influence of the growth defects on the tribological and corrosion properties will be of further interest.

Data availability

The data that support the findings in this study is available under the DOI: 10.5281/zenodo.11366794 [79] and from the corresponding author upon request.

CRediT authorship contribution statement

Julia S. Rau: Writing – review & editing, Writing – original draft, Visualization, Investigation, Funding acquisition, Formal analysis, Data curation, Conceptualization. **Gustav Eriksson:** Writing – review & editing, Investigation. **Per Malmberg:** Writing – review & editing, Investigation. **Ana Laura Puente Reyna:** Writing – review & editing, Resources, Investigation. **Jens Schwiesau:** Writing – review & editing, Resources. **Martin Andersson:** Writing – review & editing, Supervision, Resources. **Mattias Thuvander:** Writing – review & editing, Supervision, Resources.

Declaration of competing interest

The authors declare the following financial interests/personal relationships which may be considered as potential competing interests:

Ana Laura Puente Reyna and Jens Schwiesau are employees of Aesculap AG Tuttlingen, a manufacturer of orthopaedic implants.

Acknowledgments

JR gratefully acknowledges support from the Walter Benjamin fellowship [project Nr. 514540103] provided by the German Research Foundation (DFG). MA and GE acknowledge the Wallenberg Foundation and the Swedish Research Council (VR) for their support. The Aesculap AG is acknowledged for providing the analyzed material. The release for the usage of the explant was granted by Prof. Jörg Lützner, Uniklinik Dresden. This work was performed in part at the Chalmers Material Analysis Laboratory, CMAL. We thank Olof Bäcke for his support with parts of the TEM-imaging.

Supplementary materials

Supplementary material associated with this article can be found, in the online version, at doi:10.1016/j.actbio.2024.10.034.

References

[1] J.T. Evans, R.W. Walker, J.P. Evans, A.W. Blom, A. Sayers, M.R. Whitehouse, How long does a knee replacement last? A systematic review and meta-analysis of case series and national registry reports with more than 15 years of follow-up, Lancet 393 (2019) 655–663, https://doi.org/10.1016/S0140-6736(18)32531-5.
[2] P. Thomas, T. Weik, G. Roider, B. Summer, M. Thomsen, Influence of surface coating on metal ion release: evaluation in patients with metal allergy, Orthopedics 39 (2016) S24–S30, https://doi.org/10.3928/01477447-20160509-08.
[3] J. Reich, L. Hovy, H.L. Lindenmaier, R. Zeller, J. Schwiesau, P. Thomas, T. M. Grupp, Preclinical evaluation of coated knee implants for allergic patients, Orthopade 39 (2010) 495–502, https://doi.org/10.1007/s00132-009-1581-9.
[4] M. Ries, A. Salehi, K. Widding, G. Hunter, Polyethylene wear performance of oxidized zirconium and cobalt-chromium knee components under abrasive conditions, J. Bone Jt. Surg. 84 (2002) 129–135.
[5] A.L. Puente Reyna, B. Fritz, J. Schwiesau, C. Schilling, B. Summer, P. Thomas, T. M. Grupp, Metal ion release barrier function and biotribological evaluation of a zirconium nitride multilayer coated knee implant under highly demanding activities wear simulation, J. Biomech. 79 (2018) 88–96, https://doi.org/10.1016/j.jbiomech.2018.07.043.
[6] D. Cadosch, E. Chan, O.P. Gautschi, L. Filgueira, Metal is not inert: role of metal ions released by biocorrosion in aseptic loosening–current concepts, J. Biomed. Mater. Res. A 91 (2009) 1252–1262, https://doi.org/10.1002/jbm.a.32625.
[7] S.S.M. Tower, Arthroprosthetic cobaltism: neurological and cardiac manifestations in two patients with metal-on-metal arthroplasty. A case report, J. Bone Jt. Surg. 92 (2010) 2847–2851.
[8] X. Feng, J. Gu, Y. Zhou, Primary total hip arthroplasty failure: aseptic loosening remains the most common cause of revision, Am. J. Transl. Res. 14 (2022) 7080–7089.
[9] P.L. Lewis, O. Robertsson, S.E. Graves, E.W. Paxton, H.A. Prentice, A.W. Dahl, Variation and trends in reasons for knee replacement revision: a multi-registry study of revision burden, Acta Orthop. 92 (2021) 182–188, https://doi.org/10.1080/17453674.2020.1853340.
[10] S. Affatato, M. Spinelli, N. Lopomo, T.M. Grupp, M. Marcacci, A. Toni, Can the method of fixation influence the wear behaviour of ZrN coated unicompartmental mobile knee prostheses? Clin. Biomech. 26 (2011) 152–158, https://doi.org/10.1016/j.clinbiomech.2010.09.010.
[11] T. Bormann, S. Kraenzler, S. Jaeger, D. Kluess, W. Mittelmeier, T. Renkawitz, J. P. Kretzer, Stability of ceramic coatings on retrieved knee prostheses, J. Mech. Behav. Biomed. Mater. 144 (2023) 1–7, https://doi.org/10.1016/j.jmbbm.2023.105997.
[12] F. Beyer, C. Lützner, S. Kirschner, J. Lützner, Midterm results after coated and uncoated TKA: a randomized controlled study, Orthopedics 39 (2016) S13–S17, https://doi.org/10.3928/01477447-20160509-10.
[13] A.L. Puente Reyna, J. Lützner, B. Altermann, T.M. Grupp, Analysis of the *in vivo* oxidation and integrity of a zirconium nitride multilayer coated knee implant and possible effect of oxidation on the implant-cement-bone interface fixation strength, Int. Case Rep. J. 3 (2023) 1–16.

[14] S. Niyomsoan, W. Grant, D.L. Olson, B. Mishra, Variation of color in titanium and zirconium nitride decorative thin films, Thin Solid Films 415 (2002) 187–194, https://doi.org/10.1016/S0040-6090(02)00530-8.
[15] R. Brown, M.N. Alias, R. Fontana, Effect of composition and thickness on corrosion behavior of TiN and ZrN thin films, Surf. Coat. Technol. 62 (1993) 467–473, https://doi.org/10.1016/0257-8972(93)90285-V.
[16] F. Vaz, P. Carvalho, L. Cunha, L. Rebouta, C. Moura, E. Alves, A.R. Ramos, A. Cavaleiro, P. Goudeau, J.P. Rivière, Property change in ZrNxOy thin films: effect of the oxygen fraction and bias voltage, Thin Solid Films 469–470 (2004) 11–17, https://doi.org/10.1016/j.tsf.2004.06.191.
[17] Y. Cheng, Y.F. Zheng, A study of ZrN/Zr coatings deposited on NiTi alloy by PIIID technique, IEEE Trans. Plasma Sci. 34 (2006) 1105–1108, https://doi.org/10.1109/TPS.2006.877502.
[18] A.S.C.M.D. Oliveira, L. da Conceicao, The effect of oxidation on the tribolayer and sliding wear of a Co-based coating, Surf. Coat. Technol. 288 (2016) 69–78, https://doi.org/10.1016/j.surfcoat.2016.01.013.
[19] J.C.G. Milan, M.A. Carvalho, R.R. Xavier, S.D. Franco, J.D.B. De Mello, Effect of temperature, normal load and pre-oxidation on the sliding wear of multi-component ferrous alloys, Wear 259 (2005) 412–423, https://doi.org/10.1016/j.wear.2005.02.050.
[20] S.Y. Tarasov, V.E. Rubtsov, E.A. Kolubaev, A proposed diffusion-controlled wear mechanism of alloy steel friction stir welding (FSW) tools used on an aluminum alloy, Wear 318 (2014) 130–134, https://doi.org/10.1016/j.wear.2014.06.014.
[21] J.S. Rau, O. Schmidt, R. Schneider, R. Debastiani, C. Greiner, Three regimes in the tribo-oxidation of high purity copper at temperatures of up to 150°C, Adv. Eng. Mater. 24 (2022) 1–13, https://doi.org/10.1002/adem.202200518.
[22] J.S. Rau, S. Balachandran, R. Schneider, P. Gumbsch, B. Gault, C. Greiner, High diffusivity pathways govern massively enhanced oxidation during tribological sliding, Acta Mater. 221 (2021) 1–9, https://doi.org/10.1016/j.actamat.2021.117353.
[23] J. Lehmann, R. Schwaiger, M. Rinke, C. Greiner, How tribo-oxidation alters the tribological properties of copper and its oxides, Adv. Mater. Interfaces 2001673 (2020) 1–11, https://doi.org/10.1002/admi.202001673.
[24] C. Greiner, Z. Liu, L. Strassberger, P. Gumbsch, Sequence of stages in the microstructure evolution in copper under mild reciprocating tribological loading, ACS Appl. Mater. Interfaces 8 (2016) 15809–15819, https://doi.org/10.1021/acsami.6b04035.
[25] J. Li, M. Elmadagli, V.Y. Gertsman, J. Lo, A.T. Alpas, FIB and TEM characterization of subsurfaces of an Al-Si alloy (A390) subjected to sliding wear, Mater. Sci. Eng. A 421 (2006) 317–327, https://doi.org/10.1016/j.msea.2006.01.084.
[26] L. Pastewka, S. Moser, P. Gumbsch, M. Moseler, Anisotropic mechanical amorphization drives wear in diamond, Nat. Mater. 10 (2010) 34–38, https://doi.org/10.1038/nmat2902.
[27] X. Chen, Z. Han, K. Lu, Enhancing wear resistance of Cu-Al alloy by controlling subsurface dynamic recrystallization, Scr. Mater. 101 (2015) 76–79, https://doi.org/10.1016/j.scriptamat.2015.01.023.
[28] L. Bayliss, D. Culliford, A.P. Monk, S. Glyn-Jones, D. Prieto-Alhambra, A. Judge, C. Cooper, A. Carr, N. Arden, D. Beard, A. Price, The effect of patient age at intervention on risk of implant revision after total replacement of the hip or knee: a population-based cohort study, Lancet 389 (2017) 1424–1430, https://doi.org/10.1016/S0140-6736(17)30059-4.
[29] A. Kassam, P. Dieppe, A. Toms, An analysis of time and money spent on investigating painful Total Knee Replacements, Br. J. Med. Pract. 5 (2012) 1–4.
[30] Y.S. Lee, A.F. Chen, Managing bone loss in revision total knee arthroplasty, Ann. Jt. 1 (2016) 17, https://doi.org/10.21037/aoj.2016.08.03.
[31] N.D. Quinlan, V. Hegde, D.N. Bracey, A. Pollet, R.M. Johnson, D.A. Dennis, J. M. Jennings, Prevalence of depressive symptoms in aseptic revision total knee arthroplasty based on the mode of failure, Arthroplast. Today 25 (2024), https://doi.org/10.1016/j.artd.2023.101298.
[32] D. Huten, G. Pasquier, J.C. Lambotte, Techniques for filling tibiofemoral bone defects during revision total knee arthroplasty, Orthop. Traumatol. Surg. Res. 107 (2021), https://doi.org/10.1016/j.otsr.2020.102776.
[33] M. Thomsen, M. Rozak, P. Thomas, Pain in a chromium-allergic patient with total knee arthroplasty: disappearance of symptoms after revision with a special surface-coated TKA–a case report, Acta Orthop. 82 (2011) 386–388, https://doi.org/10.3109/17453674.2011.579521.
[34] T.M. Grupp, K.J. Saleh, W.M. Mihalko, M. Hintner, B. Fritz, C. Schilling, J. Schwiesau, C. Kaddick, Effect of anterior-posterior and internal-external motion restraint during knee wear simulation on a posterior stabilised knee design, J. Biomech. 46 (2013) 491–497, https://doi.org/10.1016/j.jbiomech.2012.10.017.
[35] K. Stiller, L. Viskari, G. Sundell, F. Liu, M. Thuvander, H.O. Andrén, D.J. Larson, T. Prosa, D. Reinhard, Atom probe tomography of oxide scales, Oxid. Met. 79 (2013) 227–238, https://doi.org/10.1007/s11085-012-9330-6.
[36] J. Keutgen, A.J. London, O. Cojocaru-Mirédin, Solving peak overlaps for proximity histogram analysis of complex interfaces for atom probe tomography data, Microsc. Microanal. 27 (2021) 28–35, https://doi.org/10.1017/S1431927620024800.
[37] D. Mayweg, J. Eriksson, O. Bäcke, A.J. Breen, M. Thuvander, Focused ion beam induced hydride formation does not affect Fe, Ni, Cr-clusters in irradiated Zircaloy-2, J. Nucl. Mater. 581 (2023), https://doi.org/10.1016/j.jnucmat.2023.154, 4–4.
[38] B. Gault, D.W. Saxey, M.W. Ashton, S.B. Sinnott, A.N. Chiaramonti, M.P. Moody, D. K. Schreiber, Behavior of molecules and molecular ions near a field emitter, New J. Phys. 18 (2016), https://doi.org/10.1088/1367-2630/18/3/033031.
[39] A. Devaraj, R. Colby, W.P. Hess, D.E. Perea, S. Thevuthasan, Role of photoexcitation and field ionization in the measurement of accurate oxide stoichiometry by laser-assisted atom probe tomography, J. Phys. Chem. Lett. 4 (2013) 993–998, https://doi.org/10.1021/jz400015h.
[40] Z. Yu, M. Bachhav, F. Teng, L. He, M. Dubey, A. Couet, STEM/EDS and APT study on the microstructure and microchemistry of neutron irradiated ZIRLOTM, J. Nucl. Mater. 573 (2023), https://doi.org/10.1016/j.jnucmat.2022.154139.
[41] M. Bachhav, G. Pawar, F. Vurpillot, R. Danoix, F. Danoix, B. Hannoyer, Y. Dong, E. Marquis, Interpreting the presence of an additional oxide layer in analysis of metal oxides-metal interfaces in atom probe tomography, J. Phys. Chem. C 123 (2019) 1313–1319, https://doi.org/10.1021/acs.jpcc.8b10895.
[42] I. Milošev, H.H. Strehblow, M. Gaberšček, B. Navinšek, Electrochemical oxidation of ZrN hard (PVD) coatings studied by XPS, Surf. Interface Anal. 24 (1996) 448–458, https://doi.org/10.1002/(SICI)1096-9918(199607)24:7<448::AID-SIA137>3.0.CO;2-F.
[43] I. Milošev, H.H. Strehbtow, B. Navinšek, Comparison of TiN, ZrN and CrN hard nitride coatings: electrochemical and thermal oxidation, Thin Solid Films 303 (1997) 246–254, https://doi.org/10.1016/S0040-6090(97)00069-2.
[44] D. Roman, J. Bernardi, C.L.G.D. Amorim, F.S. De Souza, A. Spinelli, C. Giacomelli, C.A. Figueroa, I.J.R. Baumvol, R.L.O. Basso, Effect of deposition temperature on microstructure and corrosion resistance of ZrN thin films deposited by DC reactive magnetron sputtering, Mater. Chem. Phys. 130 (2011) 147–153, https://doi.org/10.1016/j.matchemphys.2011.06.013.
[45] P. Prieto, L. Galán, J.M. Sanz, Interaction of oxygen with ZrN at room temperature: an XPS study, Surf. Interface Anal. 21 (1994) 395–399, https://doi.org/10.1002/sia.740210612.
[46] T. Muneshwar, K. Cadien, Comparing XPS on bare and capped ZrN films grown by plasma enhanced ALD: effect of ambient oxidation, Appl. Surf. Sci. 435 (2018) 367–376, https://doi.org/10.1016/j.apsusc.2017.11.104.
[47] P. Kontis, Z. Li, D.M. Collins, J. Cormier, D. Raabe, B. Gault, The effect of chromium and cobalt segregation at dislocations on nickel-based superalloys, Scr. Mater. 145 (2018) 76–80, https://doi.org/10.1016/j.scriptamat.2017.10.005.
[48] M. Kuzmina, M. Herbig, D. Ponge, S. Sandlobes, D. Raabe, Linear complexions: confined chemical and structural states at dislocations, Science 349 (2015) 1080–1083, https://doi.org/10.1126/science.aab2633.
[49] L. He, M. Bachhav, D.D. Keiser, J.W. Madden, E. Perez, B.D. Miller, J. Gan, W. Van Renterghem, A. Leenaers, S. Van den Berghe, STEM-EDS/EELS and APT characterization of ZrN coatings on UMo fuel kernels, J. Nucl. Mater. 511 (2018) 174–182, https://doi.org/10.1016/j.jnucmat.2018.09.004.
[50] J. Takahashi, K. Kawakami, Y. Kobayashi, Study on quantitative analysis of carbon and nitrogen in stoichiometric θ-Fe3C and γ'-Fe4N by atom probe tomography, Microsc. Microanal. 26 (2020) 185–193, https://doi.org/10.1017/S1431927620000045.
[51] Y. Qin, J. Li, M. Herbig, Microstructural origin of the outstanding durability of the high nitrogen bearing steel X30CrMoN15-1, Mater. Charact. 159 (2020) 1–15, https://doi.org/10.1016/j.matchar.2019.110049.
[52] D.A.R. Fernandez, B.S.S. Brito, I.A.D. Santos, V.F.D. Soares, A.R. Terto, G.B. de Oliveira, R. Hubler, W.W. Batista, E.K. Tentardini, Effect of hafnium contaminant present in zirconium targets on sputter deposited ZrN thin films, Nucl. Instrum. Methods Phys. Res. B 462 (2020) 90–94, https://doi.org/10.1016/j.nimb.2019.11.005.
[53] J. Mayer, L.A. Giannuzzi, T. Kamino, J. Michael, TEM sample preparation and damage, MRS Bull. 32 (2007) 400–407, https://doi.org/10.1557/mrs2007.63.
[54] J.I. Goldstein, D.E. Newbury, P. Echlin, D.C. Joy, C.E. Lyman, E. Lifshin, L. Sawyer, J.R. Michael, Scanning Electron Microscopy and X-ray Microanalysis, Springer US, Boston, MA, 2003, https://doi.org/10.1007/978-1-4615-0215-9.
[55] V. Cristaudo, K. Baert, P. Laha, M. Lyn Lim, E. Brown-Tseng, H. Terryn, T. Hauffman, A combined XPS/ToF-SIMS approach for the 3D compositional characterization of Zr-based conversion of galvanized steel, Appl. Surf. Sci. 562 (2021), https://doi.org/10.1016/j.apsusc.2021.150166.
[56] J.P. Abriata, J. Garcs, R. Versaci, The O-Zr (Oxygen-Zirconium) system, Bull. Alloy Phase Diagr. 7 (1986) 116–124.
[57] R.J. Nicholls, N. Ni, S. Lozano-Perez, A. London, D.W. McComb, P.D. Nellist, C.R. M. Grovenor, C.J. Pickard, J.R. Yates, Crystal structure of the ZrO phase at zirconium/zirconium oxide interfaces, Adv. Eng. Mater. 17 (2015) 211–215, https://doi.org/10.1002/adem.201400133.
[58] A. Yilmazbayhan, E. Breval, A.T. Motta, R.J. Comstock, Transmission electron microscopy examination of oxide layers formed on Zr alloys, J. Nucl. Mater. 349 (2006) 265–281, https://doi.org/10.1016/j.jnucmat.2005.10.012.
[59] N. Ni, S. Lozano-Perez, J. Sykes, C. Grovenor, Quantitative EELS analysis of zirconium alloy metal/oxide interfaces, Ultramicroscopy 111 (2011) 123–130, https://doi.org/10.1016/j.ultramic.2010.10.020.
[60] M. Bachhav, G. Pawar, F. Vurpillot, R. Danoix, F. Danoix, B. Hannoyer, Y. Dong, E. Marquis, Interpreting the presence of an additional oxide layer in analysis of metal oxides-metal interfaces in atom probe tomography, J. Phys. Chem. C 123 (2019) 1313–1319, https://doi.org/10.1021/acs.jpcc.8b10895.
[61] R.W. Harrison, W.E. Lee, Mechanism and kinetics of oxidation of ZrN ceramics, J. Am. Ceram. Soc. 98 (2015) 2205–2213, https://doi.org/10.1111/jace.13575.
[62] E. Ariza, L.A. Rocha, F. Vaz, L. Cunha, S.C. Ferreira, P. Carvalho, L. Rebouta, E. Alves, P. Goudeau, J.P. Rivière, Corrosion resistance of ZrNxOy thin films obtained by rf reactive magnetron sputtering, Thin Solid Films 469–470 (2004) 274–281, https://doi.org/10.1016/j.tsf.2004.08.091.
[63] S. Zhang, J. Wang, R. Wu, L. Liu, B. Pan, C. Liu, Structural and corrosion resistance properties of sputtered zirconium nitride thin films as electrode material for supercapacitor, J. Alloys Compd. 900 (2022) 1–10, https://doi.org/10.1016/j.jallcom.2021.163506.

[64] Z. Liu, T. Höche, P. Gumbsch, C. Greiner, Stages in the tribologically-induced oxidation of high-purity copper, Scr. Mater. 153 (2018) 114–117, https://doi.org/10.1016/j.scriptamat.2018.05.008.
[65] W. Tysoe, On stress-induced tribochemical reaction rates, Tribol. Lett. 65 (2017) 1–16, https://doi.org/10.1007/s11249-017-0832-x.
[66] T.E. Fischer, Tribochemistry, Ann. Rev. Mater. Sci. 18 (1988) 303–323.
[67] S.M. Hsu, J. Zhang, Z. Yin, The nature and origin of tribochemistry, Tribol. Lett. 13 (2002) 1–9, https://doi.org/10.1023/A:1020112901674.
[68] Q. Luo, Origin of friction in running-in sliding wear of nitride coatings, Tribol. Lett. 37 (2010) 529–539, https://doi.org/10.1007/s11249-009-9548-x.
[69] M. Tkadletz, C. Mitterer, B. Sartory, I. Letofsky-Papst, C. Czettl, C. Michotte, The effect of droplets in arc evaporated TiAlTaN hard coatings on the wear behavior, Surf. Coat. Technol. 257 (2014) 95–101, https://doi.org/10.1016/j.surfcoat.2014.01.010.
[70] A. Drnovšek, P. Panjan, M. Panjan, M. Čekada, The influence of growth defects in sputter-deposited TiAlN hard coatings on their tribological behavior, Surf. Coat. Technol. 288 (2016) 171–178, https://doi.org/10.1016/j.surfcoat.2016.01.021.
[71] E. Atar, E. Sabri Kayali, H. Cimenoglu, Wear behavior of As-deposited and oxidized ternary (Zr,Hf)N coatings, Metall. Mater. Trans. A 36 (2005) 2793–2800, https://doi.org/10.1007/s11661-005-0275-0.
[72] J.P. Kretzer, J. Reinders, R. Sonntag, S. Hagmann, M. Streit, S. Jeager, B. Moradi, Wear in total knee arthroplasty–just a question of polyethylene?: metal ion release in total knee arthroplasty, Int. Orthop. 38 (2014) 335–340, https://doi.org/10.1007/s00264-013-2162-4.
[73] V. Pejaković, V. Totolin, H. Göcerler, J. Brenner, M.R. Ripoll, Friction and wear behaviour of selected titanium and zirconium based nitride coatings in Na2SO4 aqueous solution under low contact pressure, Tribol. Int. 91 (2015) 267–273, https://doi.org/10.1016/j.triboint.2015.04.047.
[74] W. Cui, J. Cheng, Z. Liu, Bio-tribocorrosion behavior of a nanocrystalline TiZrN coating on biomedical titanium alloy, Surf. Coat. Technol. 369 (2019) 79–86, https://doi.org/10.1016/j.surfcoat.2019.04.036.
[75] X. Fang, A. Nakamura, J. Rödel, Deform to perform: dislocation-tuned properties of ceramics, Am. Ceram. Soc. Bull. 102 (2023) 24–29.
[76] Z.T. Wu, Z.B. Qi, D.F. Zhang, Z.C. Wang, Nanoindentation induced plastic deformation in nanocrystalline ZrN coating, Mater. Lett. 164 (2016) 120–123, https://doi.org/10.1016/j.matlet.2015.10.091.
[77] C. Greiner, Z. Liu, R. Schneider, L. Pastewka, P. Gumbsch, The origin of surface microstructure evolution in sliding friction, Scr. Mater. 153 (2018) 63–67, https://doi.org/10.1016/j.scriptamat.2018.04.048.
[78] J. Godlewski, J. Gros, M. Lambertin, J. Wadier, H. Weidinger, Raman spectroscopy study of the tetragonal-to-monoclinic transition in zirconium oxide scales and determination of overall oxygen diffusion by nuclear microanalysis of O, ASTM STP 1132 (1991) 416–436.
[79] J. Rau, G. Eriksson, P. Malmberg, A.L. Puente Reyna, J. Schwiesau, M. Andersson, M. Thuvander, Raw data to manuscript on “oxidation of a zirconium nitride multilayer covered knee implant after two years in clinical use”, Dataset (2024).